4

Advances on the Constitutive Characterization of Composites via Multiaxial Robotic Testing and Design Optimization

John G. Michopoulos

Naval Research Laboratory, Washington, DC, USA

John Hermanson

Forest Products Laboratory, Madison, WI, USA

Athanasios Iliopoulos

George Mason University, resident at NRL, Washington, DC, USA

4.1 Introduction

The research areas of mutiaxial robotic testing and design optimization have been recently utilized for the purpose of data-driven constitutive characterization of anisotropic material systems. This effort has been enabled by both the progress in the areas of computers and information in engineering as well as the progress in computational automation. Although our efforts have begun three decades ago, in this chapter we are presenting our progress on this synergistic combination of technologies developed in the last five years. Specifically, in this chapter we are reporting on the first successful implementation of our evolving methodology that recently was completed with the first industrial rate campaign of experiments for this purpose. This methodology is motivated by the data-driven requirements of employing design optimization principles for determining the constitutive behavior of composite materials as described in our recent work [1, 2].

Traditionally, the determination of the constitutive characterization of composite materials has been achieved through conventional uniaxial tests, mainly aiming for the estimation of the elastic properties. Typically, extraction of these properties, involve uniaxial tests conducted with specimens mounted on uniaxial testing machines, where the major orthotropic axis of any given specimen is angled relative to the loading direction. In addition, specimens are designed such that a homogeneous state of strain is developed over a well-defined area, which is required for the purpose of measuring stresses and strains through the measurement of the respective reaction forces and displacement [3, 4].

Consequently, the use of uniaxial testing machines imposes requirements of using multiple specimens, griping fixtures, and multiple experiments without the option of studying mutltiaxial effects. The requirement of a homogeneous state of strain frequently imposes restrictions on the sizes and shapes of specimens to be tested. These requirements result in increased cost and time, and to inefficient characterization processes.

To address these issues and to extend characterization to multiaxial state of strain in both the linear and non-linear regimes, multi-degree of freedom automated mechatronic testing machines, which are capable of loading specimens multiaxially, in conjunction with energy-based inverse characterization methodologies, were introduced at the Naval Research Laboratory (NRL) [5–7]. This development was the first of its kind and has continued through the present [8–10].

Thus, our approach employs mechatronic testing, and although it enables multiaxial loading inducing inhomogeneous states of strain, it still requires multiple specimens. However, these specimens are tested in an automated manner with high testing throughput that has recently reached a rate of 28 specimens per hour.

In addition, the recent development of flexible full-field displacement and strain measurement methods has afforded the opportunity of alternative characterization methodologies [11–14]. Full-field optical techniques, such as Moire and speckle interferometry, digital image correlation (DIC), and meshless random grid method (MRGM), which measure displacement and strain fields during mechanical tests, have been used mostly for elastic characterization of various materials [14–17]. The resulting measurements are used for identification of constitutive model constants, via the solution of an appropriately formed inverse problem, with the help of various computational techniques.

In particular, not only the authors [5–10, 14] but other groups as well [17–19] have focused on developing a mixed numerical/experimental method that identifies the material's elastic and inelastic constants by minimizing an objective function formed by the difference between the full-experimental measurements and the corresponding analytical model predictions via an optimization method.

Our approaches are based mostly on energy conservation arguments, and they can be classified according to computational cost in relation to the repetitive use of finite element analysis (FEA) or not. It is important to clarify that digitally acquired images are processed by software [20] that implements the MRGM [14, 21–25] and is used to extract the displacement and strain fields measurements as well as the boundary displacements required for material characterization. Reaction forces and redundant boundary displacement data are acquired from displacement and force sensors integrated with NRL's 6-Degrees of Freedom (6-DoF) multiaxial loader called NRL66.3 [26]. In an effort to address the computational cost of the FEA-in-the-loop approaches, the authors have initiated a dissipated and total strain energy density determination approach that has recently been extended to a framework that is derived from the total potential energy and the energy conservation, which can be applied directly with full field strain measurement for characterization [27–32].

In the section that follows we present a description of the 6-DoF loader, the associated loading space characteristics, and the experimental campaign. The following section introduces an overview of two energy-based constitutive formalisms necessary for the characterization. The implementation details of the design optimization methodology follow along with characterization, and validation results. The chapter closes with conclusions.

4.2 Automated Multiaxial Testing

4.2.1 NRL66.3: The 6–DoF Loader

NRL66.3 is a custom developed and prototyped system that represents the third generation of 6-DoF loaders built by our group. It was specifically conceived to ensure that the material to be characterized will be exposed to very general states of deformation such that the material will exhibit the most general set of strain states. The system has a recursive character because a hexapod configuration is repeated six times. This is a design decision based on our desire to satisfy a set of important requirements (mainly accumulated from previous lessons learned) in an optimum manner as described in [26]. An overview of the geometric configuration is shown in the 3-D computer aided design (CAD) representation shown in Figure 4.1a.

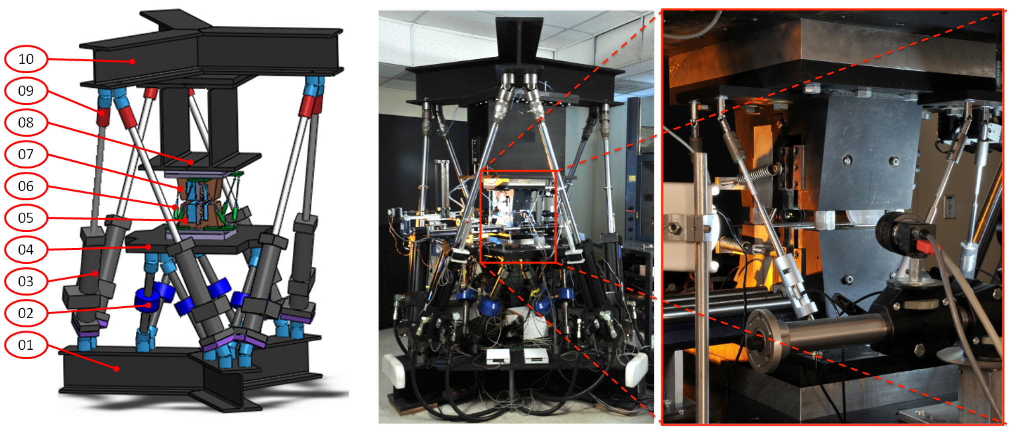

(a) Components **(b)** Long and near view

Figure 4.1: NRL66.3: 6-DoF mechatronically automated system for the multi-axial testing of composite materials: Components view (a) and long and near views of the prototype system (b).

The numbers in parentheses below are referring to the red oval labels of Figure 4.1a labeling the components of the system and they can be described as follows.

The base (01) consists of a star-shaped I-beam configuration. The angle between any two successive I-beam elements is 120 degrees.

An exact replica of the same beam configuration rotated by 60 degrees about the vertical axis of symmetry forms the top movable frame (10). The bottom base frame and the top movable frame are linked together through six actuators (03) formed by a hydraulic cylinder connecting the two frames through 12 universal joints as shown in Figure 4.1a. Each actuator consists of a main cylinder, a piston rod, an electro-hydraulic servo-valve, a magnetorestrictive position transducer, an embedded valve controller with an analog-to-digital converter for communication with the external computer.

The two frames and the six actuators define the first hexapod configuration that are forming the 6-6p linkage mechanism. By controlling the length of the actuators the 6-DoF pose of the top frame is controlled kinematically.

The base (04) supporting the lower grip (05) is connected to the fixed base (01) via a hexapod of steel rods. These rods contain at their mid-length strain gauge-based load-cells, with a capacity of 89 kN (20,000 lbf). This hexapod constitutes the second recursion.

In-line with the piston cylinders of the actuators are charge controlled piezoelectric load-cells (09) with a capacity of 220 kN (50,000 lbf) in tension and 130 kN (30,000 lbf) in compression. These load-cells constitute the third recursion of the hexapod system.

The upper grip (07) is connected to a double I-beam adapter (08) which in turn is connected to the moving frame (10). Clearly, because of this connectivity the movable grip is controlled by the motion of the top frame which is controlled by the motion of the actuators. The role of this adapter double I-beam frame is to control the location of the upper (and movable) grip in order to accommodate a particular range of specimen lengths. By shortening the height of the web on this frame taller specimens can be used for testing.

The last three recursions of the hexapod are three sets of linear displacement transducers. From inside to outside the first linear displacement transducers (06) in hexapod configuration are alternating current linear voltage displacement transducers (ACLVDTs) connecting the bases of the two grip assemblies and essentially defining the 6-DoF pose of the upper grip assembly. This is the fourth recursion of the hexapod system.

Parallel to the actuating cylinders is a set of direct current linear voltage displacement transducers (DCLVDTs) [not shown in Figure 4.1a] that are measuring the extensions of the actuator piston rods and constitute the fifth recursion of the system.

Finally, the last set of displacement transducers that are magneto-restrictive devices and are used by the actuator valve controllers for closed loop control of actuator position that are not shown in Figure 4.1a. This is the sixth and final recursion of the hexapod configuration.

Three of the hexapod recursions are stiff (actuators and two sets of load cells) and three are compliant (three sets of displacement transducers).

4.2.2 Specimen Geometry

The typical flat specimen geometry is shown in Figure 4.2 where the dark gray areas indicate the part of the specimen that is placed into the grips, and the light gray area represents the part that deforms under the influence of the applied loading. The double notches on the specimen are introduced to disturb the strain field and to ensure that some areas of the specimen (not necessarily near the notch roots) will experience non-linear constitutive response due to the corresponding strain fields. The dimensions are in the form "mm (inches)." The white dots on the deformation domain as shown in Figure 4.2(b) are markers required for measuring the displacement and strain field components via the MRGM [20, 24, 25].

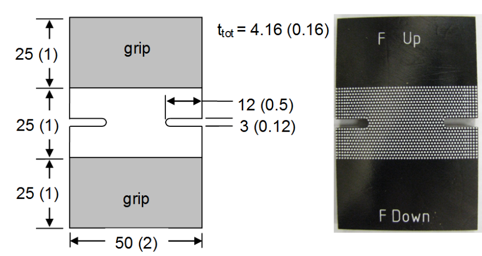

Figure 4.2: (a) Typical specimen schematic and (b) photographic view of prepared specimen.

4.2.3 Loading Space

The main mission of the system is to force the specimens under testing to develop as a complete set of strain states as possible. Consequently, it is designed such that it can be programmed to follow displacement controlled loading paths and measure boundary displacements and reaction forces and moments resulting from the mechanical response of the specimens under testing. Also, it is designed to be integrated with a pair of stereoscopic machine vision systems for capturing the surface displacements and strains in order to be used with the MRGM method for quantifying the full field strains on the surfaces of the specimens under test.

The hexapod configuration effectively converts the linear extension motions of the six actuators to the three translations and the three rotations imposed by the upper grip on the specimen. These three translations and three rotations effectively define a 6-D load space that can be sampled by commanding NRL66.3 to follow radially proportional paths and acquire data along these paths. The term proportional path here means that every path i, when represented as a vector starting in the origin and ending at point j, can be resolved to its vector space basis components in the 6-D frame $(\mathbf{u}_x, \mathbf{u}_y, \mathbf{u}_z, \mathbf{r}_x, \mathbf{r}_y, \mathbf{r}_z)$ according to

$$\mathbf{p}_i^j = p_{i1}^j \mathbf{u}_x + p_{i2}^j \mathbf{u}_y + p_{i3}^j \mathbf{u}_z + p_{i4}^j \mathbf{r}_x + p_{i5}^j \mathbf{r}_y + p_{i6}^j \mathbf{r}_z \tag{4.1}$$

where $p_{i1}^j, p_{i2}^j, p_{i3}^j, p_{i4}^j, p_{i5}^j, p_{i6}^j$ are the magnitudes of each component, and furthermore

$$p_{ik}^j = r_i^j a_{ik}^j, k \in \{1,2,3,4,5,6\}, \text{ with } a_{ik}^j = a_{ik}^{j+1} \tag{4.2}$$

A convenient parameterization of the loading paths can be obtained by invoking a transformation from the hyperspherical to its Cartesian frame of reference as follows:

$$\left.\begin{array}{l}
p_{i1}^j = r_i^j \cos(\phi_1^i) \\
p_{i2}^j = r_i^j \sin(\phi_1^i)\cos(\phi_1^i) \\
p_{i3}^j = r_i^j \sin(\phi_1^i)\sin(\phi_2^i)\cos(\phi_2^i) \\
p_{i4}^j = r_i^j \sin(\phi_1^i)\sin(\phi_2^i)\sin(\phi_3^i)\cos(\phi_3^i) \\
p_{i5}^j = r_i^j \sin(\phi_1^i)\sin(\phi_2^i)\sin(\phi_3^i)\sin(\phi_4^i)\cos(\phi_4^i) \\
p_{i6}^j = r_i^j \sin(\phi_1^i)\sin(\phi_2^i)\sin(\phi_3^i)\sin(\phi_4^i)\sin(\phi_5^i)\cos(\phi_5^i)
\end{array}\right\} \tag{4.3}$$

where r_i^j and ϕ_k^j are the magnitude of the path and the angles between it and the planes defined by the basis vectors of the 6-D kinematic space.

Affordability suggests that it is imperative that the least possible number of specimens is used to characterize a material system. Therefore, for each laminate system, we decided to use (at least) as many specimens as the number of paths used to sample the excitation space, which in this case is the loading space.

We have established that the number of paths as a function of the dimension n of the space and the number of equatorial points n_{ep} is given by [10]

$$n_{paths} = (4 + 4n_{ep})(1 + 2n_{ep})^{n-2} \tag{4.4}$$

An intermediate scenario (in terms of required number of specimens) could be based on the fact that the rotation components generate motion on the plane they are normal to. Thus, only four out of the six components can be linearly independent. In this case $n = 4$ and for $n_{ep} = 1$, Eq. 4.4 generates 72 paths. This seems to promote the solution of utilizing one of the fifteen 4-D subspaces (table 4.1) that can be used for defining the loading paths.

TABLE 4.1: Kinematic Combinations

No.	Kinematic Combination
01	u_z, r_x, r_y, r_z
02	u_y, r_x, r_y, r_z
03	u_y, u_z, r_y, r_z
04	u_y, u_z, r_x, r_z
05	u_y, u_z, r_x, r_y
06	u_x, r_x, r_y, r_z
07	u_x, u_z, r_y, r_z
08	u_x, u_z, r_x, r_z
09	u_x, u_z, r_x, r_y
10	u_x, u_y, r_y, r_z
11	u_x, u_y, r_x, r_z
12	u_x, u_y, r_x, r_y
13	u_x, u_y, u_z, r_z
14	u_x, u_y, u_z, r_y
15	u_x, u_y, u_z, r_x

A computationally intensive methodology for determining the best subspace among the 15 shown in Table 4.1 is presented in detail elsewhere [33]. An appropriate metric representation with respect to strain state volumetric histograms was developed and the notion of strain state clouds (SSCs) [33] was introduced as a means of visualizing these histograms. Extensive numerical experiments were conducted based on FEA computations of the elastic response of a composite specimen with edge notches. They were used as the means for generating all possible strain states generated by loading paths in corresponding sub-spaces. A typical example of the relevant SSCs is depicted in Figs.4.3c, 4.3d for loading case 02 (u_y, r_x, r_y, r_z) and in Figs. 4.3c, 4.3d for the loading case 15 (u_x, u_y, u_z, r_x). The color scale from blue to red indicates the distance from $\{0,0,0\}$ and is only used as a visual aid assisting qualitative comparison.

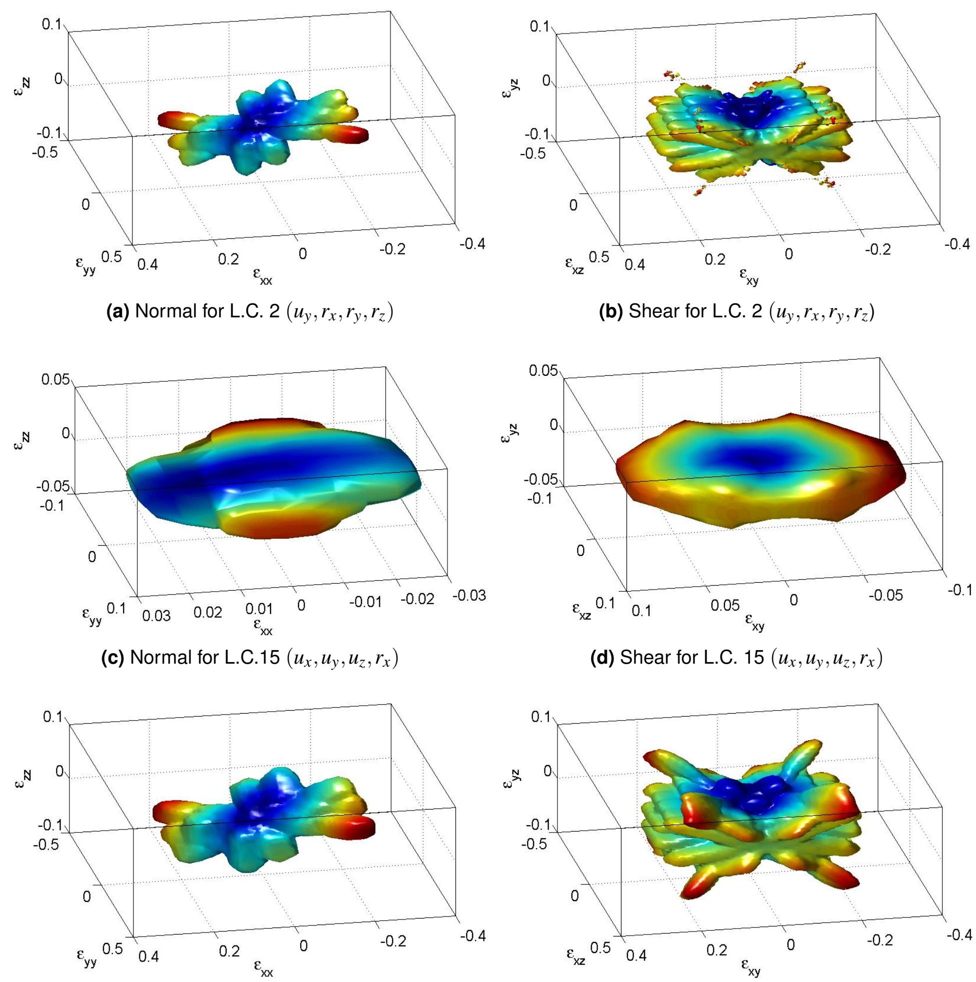

(a) Normal for L.C. 2 (u_y, r_x, r_y, r_z)

(b) Shear for L.C. 2 (u_y, r_x, r_y, r_z)

(c) Normal for L.C.15 (u_x, u_y, u_z, r_x)

(d) Shear for L.C. 15 (u_x, u_y, u_z, r_x)

(e) Normal for all loading combinations

(f) Shear for all loading combinations

Figure 4.3: Normal and Shear Strain State Clouds for a specimen with stacking sequence $[-30°, 30°]_{16}$

The ratio of the volume of each SSC relative to the union of the volumes of all SSCs created by all possible loading paths within all subspaces as shown in Figs. 4.3e, 4.3f, was used as the load subspace ranking metric. It was established that the subspaces involving all three rotations and one of the two in-plane translations generate the richest strain state sets (cases 2 and 6).

As these two top cases are actually found to be very close with regard to the richness of the generated strain states, and the design of the NRL66.3 promotes the least amount of energy losses for case 6, this was the final subspace selected to reflect the 4-D subspace required to be sampled by the 72 loading paths described for the conducted experiments.

A view of any 4-D ball and its corresponding 3-dimensional sphere in terms of its 3-D projections for the cases of the parallel circles, the hypermeridians, and the meridians is shown in Figure 4.4.

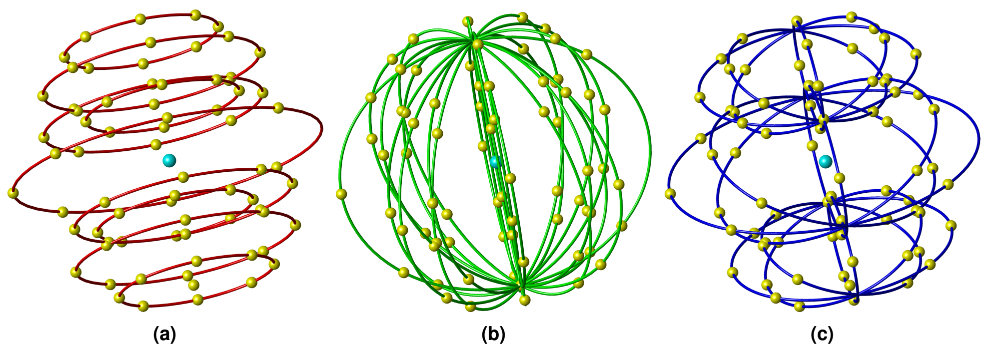

Figure 4.4: 3-D projections of a 3-D hypersphere defining the utilized loading space. Each projection shows (a) the corresponding parallel circles, (b) the hypermeridians and (c) the meridians involved.

The smaller yellow spheres represent the intersections of these three projections when combined, and reflect the instantaneous end of the 72 vector paths originating from the center denoted by the cyan sphere.

4.2.4 Experimental Campaign

The lowest number of specimens used based on economical considerations was determined by using a single specimen per loading path. For reasons of simple redundancy we decided to repeat each path, and therefore each load path was followed twice by testing two specimens of identical material system. Thus 144 specimens per material system are required. Each material system was defined to be a balanced laminate with an alternating angle of fiber inclination per ply relative to the vertical axis of the specimen that is perpendicular to the axis defined by the two notches of the specimen. Four angles were used, $+/-15, +/-30, +/-60, +/-75$ degrees, and therefore $4 \times 144 = 576$ specimens were constructed. The actual material used to make the specimens was an AS4/3506-1 epoxy resin/fiber.

However, because we needed to study ply thickness length scale effects, we constructed an equal amount of specimens where the cross-plied unidirectional laminas were made with four plies each, thus leading to thicker uniaxial laminas. This doubled the number of total specimens to 1,152 and this was the final number of required tests. All specimens were tested by using NRL66.3 in May of 2011. A very small sample of the testing process is shown in a movie that can be found at URL `http://www.youtube.com/watch?v=Cp18y3HAqsM`. In May 13, 2011, the system achieved a throughput of 20 tests/hour for a total of 132 tests. On May 27, the system achieved a throughput of 25 tests/hour for a total of 216 tests. On June 15, 2011, the system reached its peak throughput of 28 tests/hour. All 1,152 tests were completed in 12 workdays. The test yielded 13 TB of data from the sensors and the cameras of the system.

Instead of presenting typical load-displacement curves representing collected data in a 12-dimensional space (i.e. three forces and three moments vs. three translations and three rotations respectively) it is more convenient and descriptive to present total energy distribution as a function of load increment (frame no.) along the respective loading path as shown in Figure 4.5.

The measurement of the loads and displacements at the boundaries of the specimens during the tests enable the computation of the total energy evolution as well as its decompositional parts, as shown for two different examples in Figure 4.5 by using the procedure described in section 4 of [7]. What is of interest in these two graphs is the distinctly different response of the specimen. In Figure 4.5a the energy evolution for a $+/-15$ specimen exposed to a combination of compression, positive bending, and in-plane rotation, while Figure 4.5b a $+/-30$ specimen is exposed to a combination of compression, negative bending, and negative torsion. While the first specimen begins softening due to damage accumulation as shown by the very early at about the 270th frame departure from zero of the dissipated energy. The second figure exhibits a late and very abrupt initiation and evolution of softening at about frame 298 as the respective energy dissipation line indicates.

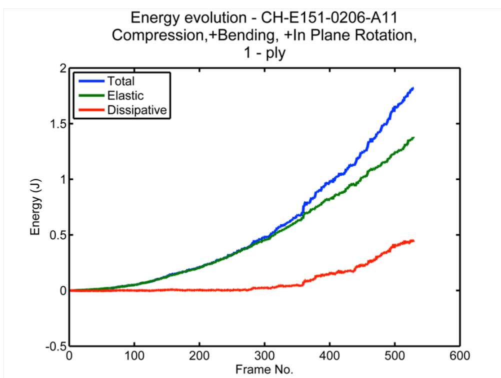

(a)

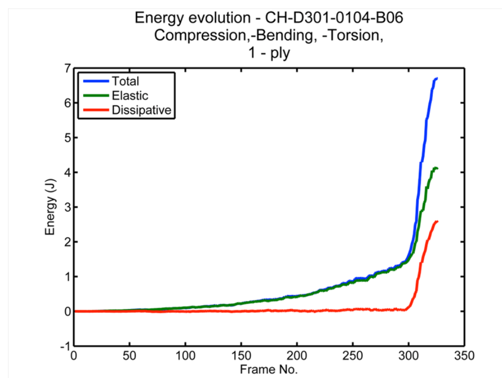

(b)

Figure 4.5: Evolution of total, elastic, and dissipated energy for two distinct load paths.

4.3 Constitutive Formalisms

The mathematical form of the constitutive behavior of a general anisotropic material has been selected to be the one that can be extracted by the adoption of a modified anisotropic hyperelastic strain energy density function that can be constructed to encapsulate both the elastic and the inelastic responses of the material. However, certain classes of composite materials reach failure after small strains and some under large strains. For this reason we adopted two cases, one involving a small (infinitesimal) strain formulation (SSF) and another involving a finite (large) strain formulation (FSF).

4.3.1 Small Strain Formulation

For the SSF we introduce a strain energy density (SED) function that, in its most general form, can be represented as a scaled Taylor expansion of the Helmholtz free energy of a deformable body, which is in terms of small strain invariants of the form,

$$\begin{aligned} U_{SSF}(I_1,I_2,I_3) = s_0 + s_{11}I_1 + \frac{1}{2}s_{12}I_1^2 + \frac{1}{3!}s_{13}I_1^3 + \frac{1}{4!}s_{14}I_1^4 + \ldots + s_{21}I_2 + \frac{1}{2}s_{22}I_2^2 + \frac{1}{3!}s_{23}I_2^3 + \frac{1}{4!}s_{24}I_2^4 + \\ + \ldots + \frac{1}{2}s_{13}I_3^2 + \frac{1}{3!}s_{13}I_3^3 + \frac{1}{4!}s_{14}I_3^4 \ldots + \frac{1}{2}s_{1121}I_1I_2 + \frac{1}{3!}s_{1221}I_1^2I_2 + \frac{1}{3!}s_{1122}I_1I_2^2 + \ldots + \\ + \frac{1}{2}s_{1131}I_1I_3 + \frac{1}{3!}s_{1331}I_1^2I_3 + \frac{1}{3!}s_{1133}I_1I_3^2 + \ldots + \frac{1}{4!}s_{1321}I_1^3I_2 + \frac{1}{4!}s_{1221}I_1^2I_2^2 + \frac{1}{4!}s_{1123}I_1I_2^3 + \ldots, \end{aligned} \tag{4.5}$$

where the invariants are defined by:

$$I_1 = tr(\varepsilon) = \varepsilon_{ii};\;\; I_2 = \frac{1}{2}tr(\varepsilon^2) = \frac{1}{2}\varepsilon_{ij}\varepsilon_{ij};\;\; I_3 = \frac{1}{2}tr(\varepsilon^3) = \frac{1}{3}\varepsilon_{ij}\varepsilon_{jk}.\varepsilon_{ki}. \tag{4.6}$$

The invariants are chosen to take advantage of a priori knowledge that the SED as a scalar quantity must be invariant under frame reference translations and rotations. This follows in that the SED should be objective (i.e., independent of the observer's frame of reference). An additive decomposition of this expression in terms of a recoverable and an irrecoverable SED can be expressed by:

$$U_{SSF} = U^R_{SSF}(S;\varepsilon_{ij}) + U^I_{SSF}(D;\varepsilon_{ij}). \tag{4.7}$$

The second-order monomials of strain components will be forming the recoverable part $U^R_{SSF}(S;\varepsilon_{ij})$ and the higher-order monomials will be responsible for the irrecoverable part $U^I_{SSF}(D;\varepsilon_{ij})$. The resulting constitutive law is given by:

$$\begin{aligned} \sigma_{ij} = \partial U_{SSF}/\partial\varepsilon_{ij} = \partial(U^R_{SSF}(S;\varepsilon_{ij}) + U^I_{SSF}(D;\varepsilon_{ij}))/\partial\varepsilon_{ij} = \\ = \frac{\partial U_{SSF}}{\partial I_1}\frac{\partial I_1}{\partial\varepsilon_{ij}} + \frac{\partial U_{SSF}}{\partial I_2}\frac{\partial I_2}{\partial\varepsilon_{ij}} + \frac{\partial U_{SSF}}{\partial I_3}\frac{\partial I_3}{\partial\varepsilon_{ij}}. \end{aligned} \tag{4.8}$$

A general expression that provides a strain dependent version of Eq. 4.7, is given by,

$$U_{SSF} = U^R_{SSF}(S;\varepsilon_{ij}) + U^I_{SSF}(D;\varepsilon_{ij}) = \frac{1}{2}s_{ijkl}\varepsilon_{ij}\varepsilon_{kl} + d_{ijkl}(\varepsilon_{ij})\varepsilon_{ij}\varepsilon_{kl}, \tag{4.9}$$

where s_{ijkl} are the components of the elastic stiffness tensor (Hooke's tensor) and $d_{ijkl}(\varepsilon_{ij})$ are strain-dependent damage functions, which fully define the irrecoverable or dissipated strain energy density given by enforcing the dissipative nature of energy density. The quantity $d_{ijkl}(\varepsilon_{ij})$ can be defined in a manner analogous to that employed for the one-dimensional system described in [1] and is given by:

$$d_{ijkl}(\varepsilon_{ij}) = s_{ijkl}(1 - e^{(-\frac{\varepsilon_{ij}}{q_{ij}})^{p_{ij}}/(ep_{ij})}). \tag{4.10}$$

We perform an equivalent series expansion and subsequently drop all terms except the first, in that it captures almost all of the dissipative behavior. Accordingly:

$$d_{ijkl}(\varepsilon_{ij}) = s_{ijkl}\sum_{m=1}^{n}(-1)^m\left(\frac{1}{ep_{ij}}\right)^m\frac{\varepsilon_{ij}^{mp_{ij}}}{m!q_{ij}^{mp_{ij}}} \simeq -s_{ijkl}\left(\frac{1}{ep_{ij}}\right)\frac{\varepsilon_{ij}^{p_{ij}}}{q_{ij}^{p_{ij}}}. \tag{4.11}$$

Thus the irrecoverable part of the energy density in Eq. 4.7 becomes:

$$U^I_{SSF}(D;\varepsilon_{ij}) = U^I_{SSF}(s_{ijkl},p_{ij},q_{ij};\varepsilon_{ij}) = -s_{ijkl}\frac{1}{e(2+p_{ij})p_{ij}q_{ij}^{p_{ij}}}\varepsilon_{ij}^{1+p_{ij}}\varepsilon_{kl}. \tag{4.12}$$

Next, substituting Eq. 4.12 into Eq. 4.9 yields:

$$U_{SSF} = U_{SSF}^{R}(S;\varepsilon_{ij}) + U_{SSF}^{I}(D;\varepsilon_{ij}) = \frac{1}{2} s_{ijkl}\varepsilon_{ij}\varepsilon_{kl} - s_{ijkl}\frac{1}{e(2+p_{ij})p_{ij}q_{ij}^{p_{ij}}}\varepsilon_{ij}^{1+p_{ij}}\varepsilon_{kl}. \tag{4.13}$$

Applying Eq. 4.6 on Eq. 4.11, and employing Voigt [3] notation for the case of a general orthotropic material, yields the constitutive relation,

$$\begin{bmatrix} \sigma_{xx} \\ \sigma_{yy} \\ \sigma_{zz} \\ \sigma_{xz} \\ \sigma_{yz} \\ \sigma_{xy} \end{bmatrix} = \begin{bmatrix} \breve{s_{xx}} & s_{xy} & s_{xz} & 0 & 0 & 0 \\ s_{xy} & \breve{s_{yy}} & s_{yz} & 0 & 0 & 0 \\ s_{xz} & s_{yz} & \breve{s_{zz}} & 0 & 0 & 0 \\ 0 & 0 & 0 & \breve{s_{xz}} & 0 & 0 \\ 0 & 0 & 0 & 0 & \breve{s_{yz}} & 0 \\ 0 & 0 & 0 & 0 & 0 & \breve{s_{xy}} \end{bmatrix} \begin{bmatrix} \varepsilon_{xx} \\ \varepsilon_{yy} \\ \varepsilon_{zz} \\ \varepsilon_{xz} \\ \varepsilon_{yz} \\ \varepsilon_{xy} \end{bmatrix}, \tag{4.14}$$

where,

$$\breve{s_{ij}} = s_{ij}\left(1-\bar{d_{ij}}\right) \tag{4.15}$$

and

$$\bar{d_{ij}} = \frac{1}{e p_{ij} q_{ij}^{p_{ij}}}\varepsilon_{ij}^{1+p_{ij}}. \tag{4.16}$$

The othotropic symmetry requirement enforce the zero terms in the generalized Hooke's expression in Eq. 4.14. Therefore, the material parameters are the 9 elastic s_{ij} constants and $6\times 2 = 12$ damage constants p_{ij}, q_{ij} amounting to a total of 21 parameters. Clearly, when the quantities $\bar{d_{ij}}$ do not depend on the strains and they are constants, Eq. 4.12 reduces to most of the continuous damage theories given by various investigators in the past [34–37]. For a transversely isotropic material the number of material parameters drops to 5+10=15 for a 3-D state of strain and to 4+8=12 for a plane stress state.

4.3.2 Finite Strain Formulation

The FSF can be written in a double additive decomposition manner. The first being the decomposition of the recoverable and irrecoverable SED, and the second being the decomposition between the volumetric (or dilatational) W_v and the distortional (or isochoric) W_d parts of the total SED. This decomposition is expressed by,

$$\begin{aligned} U_{FSF} &= U_{FSF}^{R}(\alpha_i;J,\bar{C}) + U_{FSF}^{I}(\alpha_i,\beta_i;J,\bar{C}) = \\ &= [W_v(J) + W_d(\bar{C},A\otimes A,B\otimes B)] - [d_v W_v(J) + d_d W_d(\bar{C},A\otimes A,B\otimes B)], \end{aligned} \tag{4.17}$$

where α_i,β_i are the elastic and inelastic material parameters of the system, respectively. A rearrangement of these decompositions, such as the volumetric vs. distortional decomposition, which appears on the highest expression level, leads to an expression introduced in [38], i.e.,

$$U_{FSF} = (1-d_v)W_v(J) + (1-d_d)W_d(\bar{C},A\otimes A,B\otimes B), \tag{4.18}$$

with the damage parameters $d_k \in [0,1], k \in [v,d]$ defined as,

$$d_k = d_{ka}^{\infty}\left[1 - e^{\left(-\frac{a_k(t)}{\eta_{ka}}\right)}\right], \tag{4.19}$$

where $a_k(t) = \max\limits_{s\in[0,t]} W_k^o(s)$ is the maximum energy component reached so far, and $d_{ka}^{\infty}, \eta_{ka}$ are two pairs of parameters controlling the energy dissipation characteristics of the two components of SED. In this formulation, $J = \det \underline{F}$ is the determinant of the deformation gradient, $\bar{C} = \underline{F}^T\underline{F}$ is the right

Cauchy-Green (Green deformation) tensor, A, B are constitutive material directions in the undeformed configuration, and $A \otimes A, B \otimes B$ are microstructure structural tensors expressing fiber directions. Each of the two components of SED are defined as,

$$\begin{aligned} W_v(J) &= \frac{1}{d}(J-1)^2 \\ W_d(\bar{C}, A \otimes A, B \otimes B) &= \sum_{i=1}^{3} a_i(\bar{I}_1 - 3)^i + \sum_{j=1}^{3} b_j(\bar{I}_2 - 3)^j + \sum_{k=1}^{6} c_k(\bar{I}_4 - 1)^k + \\ + \sum_{l=2}^{6} d_l(\bar{I}_5 - 1)^l + \sum_{m=2}^{6} e_m(\bar{I}_6 - 1)^m &+ \sum_{n=2}^{6} f_n(\bar{I}_7 - 1)^n + \sum_{o=2}^{6} g_o(\bar{I}_8 - (A \cdot B)^2)^o, \end{aligned} \tag{4.20}$$

where the strain invariants are defined as follows:

$$\begin{aligned} &\bar{I}_1 = tr\bar{C},\ \ \bar{I}_2 = \tfrac{1}{2}(tr^2\bar{C} - tr\bar{C}^2) \\ &\bar{I}_4 = A \cdot \bar{C}B,\ \ \bar{I}_5 = A \cdot \bar{C}^2 B \\ &\bar{I}_6 = B \cdot \bar{C}B,\ \ \bar{I}_7 = B \cdot \bar{C}^2 B,\ \ \bar{I}_8 = (A \cdot B)A \cdot \bar{C}B. \end{aligned} \tag{4.21}$$

The corresponding constitutive behavior is given by the second Piola-Kirchhoff stress tensor according to [35]:

$$S = 2\frac{\partial U_{FSF}}{\partial C}. \tag{4.22}$$

or the usual Cauchy stress tensor according to:

$$\sigma_{FSF} = \frac{2}{J} F \cdot \frac{\partial U_{FSF}}{\partial C} \cdot F^T. \tag{4.23}$$

Under the FSF the material characterization problem involves determining the 36 coefficients (at most) of all monomials when the sums in the expression of distortional SED are expanded in Eq. 4.20, in addition to the compressibility constant d and the 4 parameters used in Eq. 4.19. It follows that potentially there can be a total of 41 material constants.

4.4 Design Optimization

4.4.1 Computational Implementation

In order to determine the material parameters the inverse problem at hand is solved through a design optimization approach that is described by the logic depicted in Figure 4.6a.

The implementation of this logic involved a computational infrastructure that was controlled by Matlab, where the foreword solution of the instantaneous FEA was accomplished by ANSYS. Due to the costly calculations we created a virtual cluster that essentially used the multiple cores available in three systems, via an on-demand spawning of 102 virtual machines capable of running 102 instances of ANSYS in a parallel fashion, whereas each process was responsible for searching in a different subdomain of the design space. An overview of the adopted architecture is shown in Figure 4.6b.

Details of the FEM model used for the specimens constructed and tested are not presented here due to the space limitations but they can be found in [1, 2].

Two objective functions were constructed. Both utilized the fact that through the REMDIS-3D software [39], developed by our group, one can obtain full field measurements of the displacement and strain fields over any deformable body as an extension of the REMDIS-2D software that is based on the MRGM [14, 20–25]. Thus, our experimental measurements for the formation of the

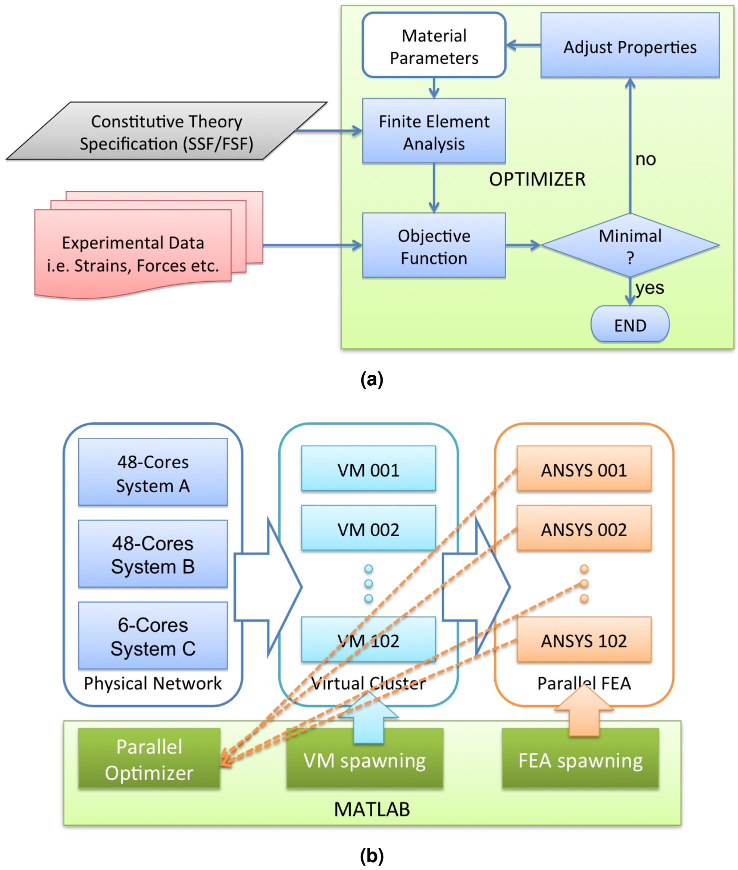

Figure 4.6: Design optimization logic implementation (a), and virtualized compute cluster architecture for implementing the optimization in parallel (b)

objective functions were chosen to be the strains at the nodal points of the FEM discretization. The first objective function chosen was based entirely on strains and is given by,

$$J^{\varepsilon} = \sum_{k=1}^{N} \sum_{i=1}^{2} \sum_{j=i}^{2} \left(\left[\varepsilon_{ij}^{\exp} \right]_k - \left[\varepsilon_{ij}^{fem} \right]_k \right) \Bigg)^2 , \tag{4.24}$$

the second objective function is given in terms of surface strain energy density according to,

$$\begin{aligned} J^U \approx \oint_{\partial\Omega} \left(U^{\exp} - U^{fem} \right)^2 dS \approx \\ \approx \oint_{\partial\Omega} \sum_{i=1}^{2} \sum_{j=i}^{2} \sum_{m=1}^{2} \sum_{n=m}^{2} \left(s_{ijmn} \varepsilon_{ij}^{\exp} \varepsilon_{mn}^{\exp} - s_{ijmn} \varepsilon_{ij}^{fem} \varepsilon_{mn}^{fem} \right) \Bigg)^2 dS, \end{aligned} \tag{4.25}$$

where $\left[\varepsilon_{ij}^{\exp} \right]_k, \left[\varepsilon_{ij}^{fem} \right]_k$ are the experimentally determined and the FEM produced components of strain at node k. The quantities $U^{\exp}$,U^{fem} are the surface strain energy densities formulated by using the experimental strains and the FEM produced strains, respectively. Both objective functions were implemented, and we utilized both the DIRECT global optimizer [40], which is available within Matlab [41], and a custom developed Monte-Carlo optimizer, also implemented in Matlab.

For the case of the FSF a two-stage optimization was performed. In the first stage, we determined the values of the coefficients of the strain invariant monomials in Eq. 4.20 such that the FSF matches the SSF by constructing and minimizing an objective function of the form

$$J^{URF}(d,a_1,b_1,c_1,d_1) \approx \oint_{\partial\Omega} \left(U^R_{FSF} - U^R_{SSF}\right)^2 dS \approx \\ \approx \left[\oint_{\partial\Omega} \left(\sum_{i=1}^{2}\sum_{j=i}^{2}\sum_{m=1}^{2}\sum_{n=m}^{2} \left(U^R_{FSF} - U^R_{SSF}\right) \right)^2 dS \right] \tag{4.26}$$

This was done is order to establish the proper parameters of the FSF model that match the SSF model.

In the second stage, the material parameters encoding the damage behavior of the FSF were determined through the minimization of the objective function

$$J^{UF}(d,a_1,b_1,c_1,d_1,d_a^{\infty},\eta_a) \approx \oint_{\partial\Omega} \left(U^1_{FSF} - U^2_{FSF}\right)^2 dS \approx \\ \approx \left[\oint_{\partial\Omega} \left(\sum_{i=1}^{2}\sum_{j=i}^{2}\sum_{m=1}^{2}\sum_{n=m}^{2} \left(U^1_{FSF} - U^2_{FSF}\right) \right)^2 dS \right] \tag{4.27}$$

where $U^1_{FSF}(\bar{d},\bar{a}_1,\bar{b}_1,\bar{c}_1,\bar{d}_1,\bar{d}_a^{\infty},\bar{\eta}_a)$ is the SED of the FSF for the parameters $\bar{d},\bar{a}_1,\bar{b}_1,\bar{c}_1,\bar{d}_1$ computed from the previous step of matching the FSF with the SSF. This complete set of parameters represents the known target model of the material as shown in the second row of Table 4. The unknown constitutive model was chosen to be represented by another FSF SED, namely $U^1_{FSF}(d,a_1,b_1,c_1,d_1,d_a^{\infty},\eta_a)$.

4.4.2 Design Optimization Numerical Results

For the purpose of demonstrating numerically the effectiveness of the aforementioned design optimization concepts, the material selected for generating the necessary simulated experimental data is a typical laminate constructed from an epoxy resin/fiber lamina system of type AS4/3506-1. The elastic moduli of this material are listed in Table 4.2 according to several sources [3, 42–44]

Clearly, for what is considered to be a set of material constants their values vary widely. This can be attributed to the fact that these properties really depend on many factors such as the fiber volume fraction, the fiber coating, the manufacturing process of the fiber, resin and composite, and the quality of the experimental procedure overall. As can be seen from the bottom entries of the table where we added some statistical observations, % deviation observed varies from 11.1 % to 78.2 %. It is therefore important to identify the set of elastic material properties before and after a batch of new material is manufactured or before a material system is used for design, material qualification or material certification. To demonstrate the usage of the SSF in conjunction with design optimization we present here an example of using real data from a multi-axially loaded specimen from a test conducted by utilizing NRL66.3. The model characteristics of the specimen used are presented in Figure 4.7, where in Figure 4.7a the discretization model and potential boundary conditions are depicted, and in Figure 4.7b, a detail in the area of the left notch shows a stacking of [+60,-60]16 with each lamina made out of AS4/3506-1.

The bottom row of Table 4.3 shows the parameters determined by minimizing the objective function in Eq. 4.27 via a Monte-Carlo global optimizer developed in-house.

TABLE 4.2: Engineering properties of AS4/3506-1 laminae

Ref.	E_{11} [GPa]	E_{22} [GPa]	E_{33} [GPa]	ν_{12}	ν_{23}	ν_{13}	G_{12} [GPa]	G_{23} [GPa]	G_{13} [GPa]
[3]	147.0	10.3	10.3	0.27	0.28	0.27	7.0	4.04	7.0
[42]	142.0	9.8	9.8	0.30	0.34	0.30	6.0	3.77	6.0
[43]	135.0	9.0	9.0	0.28		0.28	6.9		6.9
[44]	138.0	9.7	9.7	0.30	0.49	0.30	5.24	3.24	5.24
[45]	139.3	11.1	11.1	0.30	0.40	0.30	6.0	3.964	6.0
[46]	150.0	8.0	8.0	0.30		0.30	5.0		5.0
[47]	147.0	10.3	10.3	0.27		0.27	6.89		6.89
[48]	142.0	10.3	10.3	0.27		0.27	7.2		7.2
Min	135.0	8.0	8.0	0.27	0.28	0.27	5.0	3.24	5.0
Avg.	142.5	9.8	9.8	0.29	0.30	0.29	6.279	3.753	6.279
Max.	150.0	11.1	11.1	0.30	0.49	0.30	7.2	4.039	7.2
Deviation [%]	11.1	38.8	38.8	11.1	78.2	11.1	44.0	24.7	44.0
Avg. Cons.	142.5	9.81	9.81	0.29	0.30	0.29	6.279	3.769	6.279

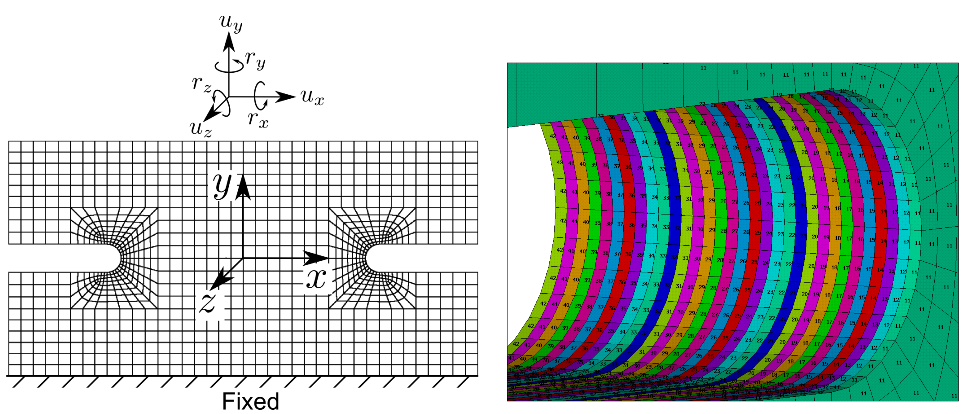

(a) Discretization and boundary conditions of typical specimen used for material characterization

(b) Detail of FEA model near one of the notches

Figure 4.7: Finite Elements Model

TABLE 4.3: FSF parameters of AS4/3506-1 laminae with damage

Model	d	a_1	b_1	c_1	e_1	d_a^∞	η_a
Target	0.00007012	1,611	713	29,212	-458.7	0.9	1.8
Identified	0.00006987	1,613	721	29,105	-449.3	0.92	1.979

An indication of how well the FSF can capture the SSF, for the case of the recoverable (linear elastic) regime, is shown in Figure 4.8, where the distribution of ε_{yy} is shown for both models for a case of combined torsion and tension of the specimen. In addition, a comparison of load vs. strain evolution, for a point in front of the first of two notches, is shown in Figure 4.9.

Using the collected data and the optimization approach outlined earlier for the case of the SSF we identified the elastic constants as shown in Table 4.4, in comparison to those of [3]. By running FEA

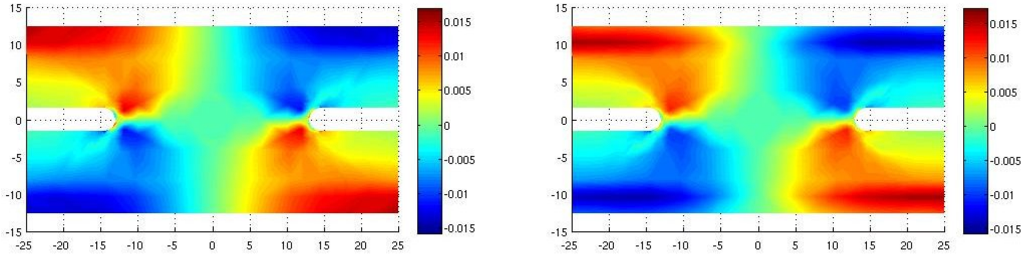

(a) Small strain formulation FEA results

(b) Finite strain formulation FEA results

Figure 4.8: FEA results of the vertical component of strain (ε_{yy}) for the case of a specimen loaded both in tension and torsion

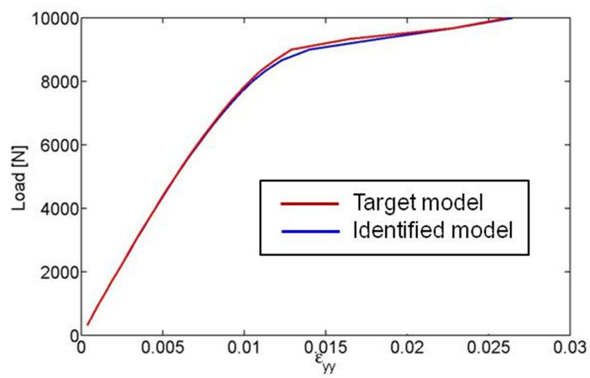

Figure 4.9: Comparison of the load vs. vertical component of strain (ε_{yy}) at a point in front of the notch, between the target and the identified model, by using the FSF

TABLE 4.4: Engineering properties of AS4/3506-1 laminae

Ref	E_{11}[GPa]	E_{22} [GPa]	ν_{12}	ν_{23}	G_{12}[GPa]
Daniels [3]	147.0	10.3	0.27	0.28	7.0
Present	125.0	10.8	0.27	0.32	7.96

for the cases that correspond to the specific loading path corresponding to an experiment we can now compare the predicted distribution of any component of the strain or stress tensor. In order to demonstrate how well the FSF formulation can capture the behavior of the characterization coupons used to obtain the data utilized in the characterization process, we are presenting typical examples in terms of the distributions of ε_{yy} as measured by the MRGM (left column) and as predicted by the FSF theory (right column), for both the front (top row) and the back (bottom row) of Figs. 4.10, 4.11, 4.12, and 4.13.

It is important to mention that the characterization methodology described here and in our previous publications utilized the data described herein, along with the data from other validation tests performed on structures of different shape and layups than those of the characterization coupons, to perform validation comparisons. A discussion of this activity is briefly presented in the next section and in more extended form in [49].

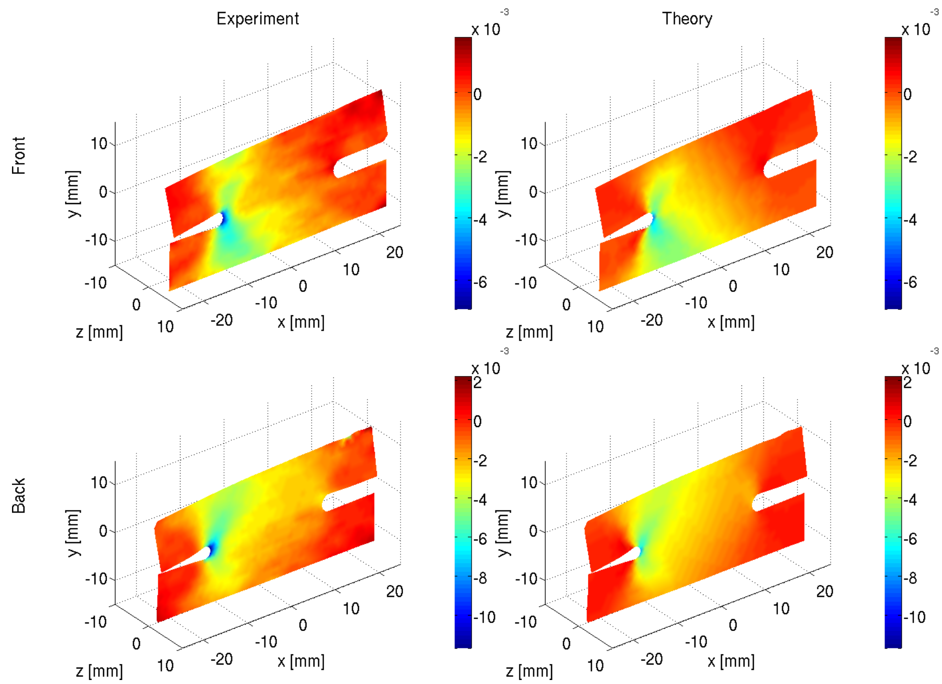

Figure 4.10: Comparison of (ε_{yy}) field between measured (left) and the identified model by using the FSF for the case of compression and in-plane rotation of a +/- 30 degrees laminate

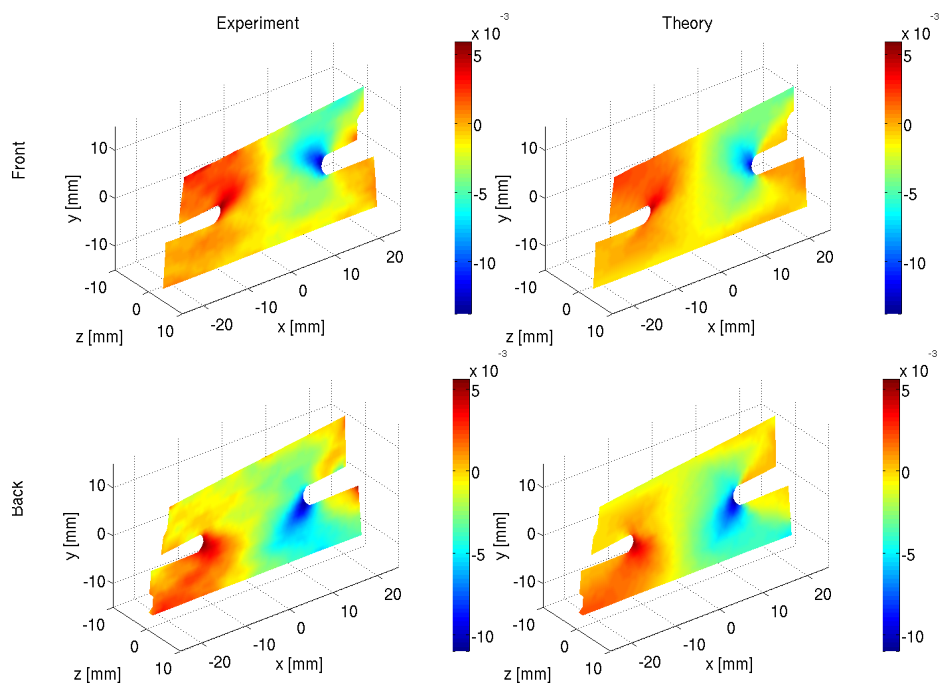

Figure 4.11: Comparison of (ε_{yy}) field between measured (left) and the identified model by using the FSF for the case of in-plane rotation and torsion of a +/- 60 degrees laminate

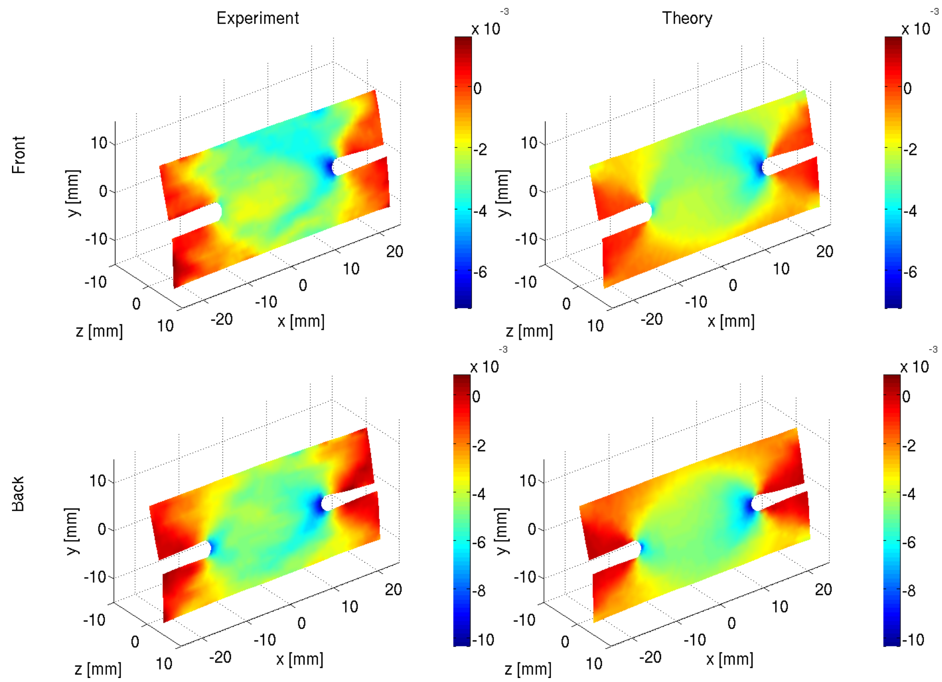

Figure 4.12: Comparison of (ε_{yy}) field between measured (left) and the identified model by using the FSF for the case of compression, bending, and negative in-plane rotation of a +/- 60 degrees laminate

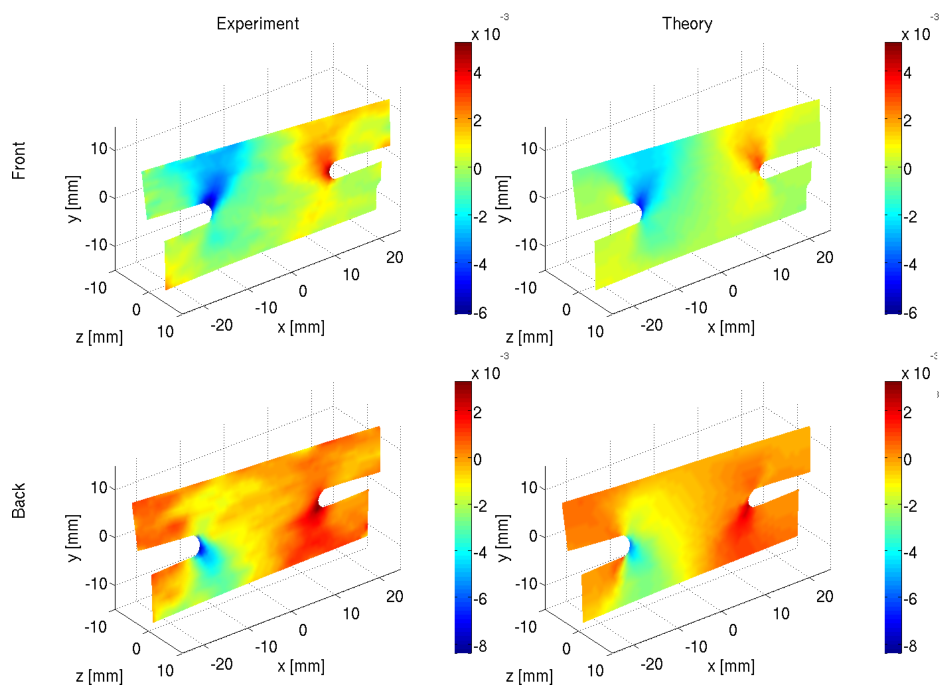

Figure 4.13: Comparison of (ε_{yy}) field between measured (left) and the identified model by using the FSF for the case of bending, in-plane rotation, and torsion of a +/- 30 degrees laminate with four-plies per layer

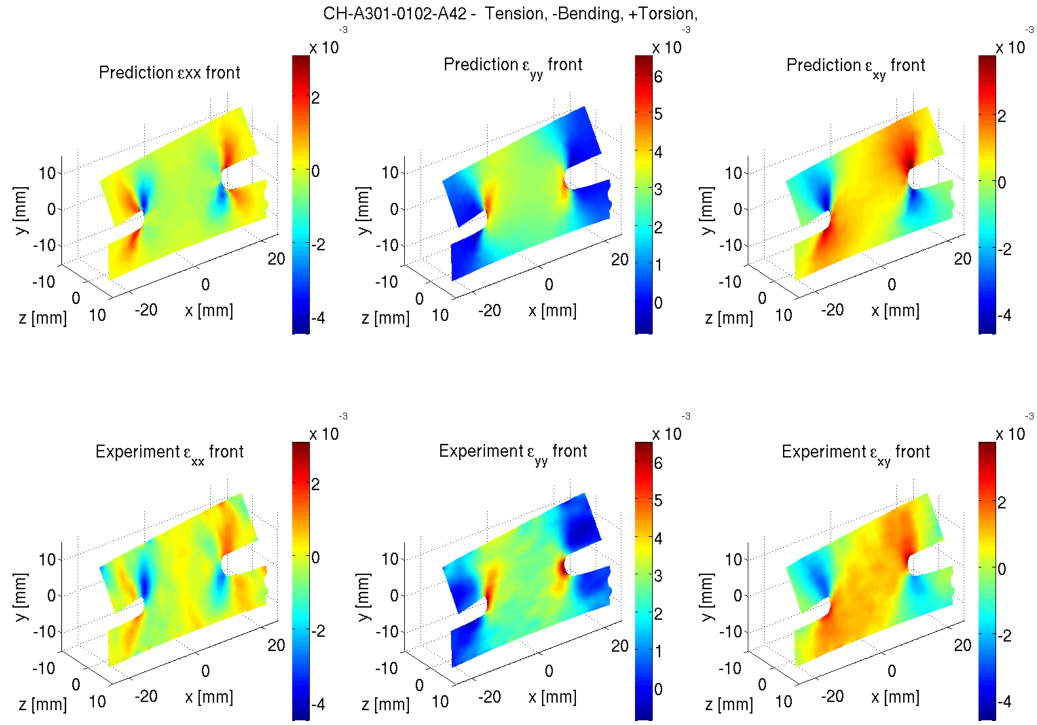

Figure 4.14: Predicted (top row) vs. experimental (bottom row) strain component fields distributions for a characterization coupon under combined tension, bending and torsion loading

4.5 Validation

The first validation simulation were performed for the typical double-notched characterization specimen described elsewhere [50], but for loading paths that were not used for determining the constitutive model itself.

For the sake of brevity, we will not describe here the details of the geometry and layup configuration nor the details of the full 3-D FEA model used for behavior predictions of the characterization specimens. The FSF formulation was used and the material parameters used were those identified by the design optimization process and described in Table 4.3.

As a representative validation prediction we are presenting the results for two loading paths. It is important to emphasize that the experimental data obtained from the associated tests were not used in determining the constitutive constants (material parameters) that are fixing the associated constitutive model.

Figure 4.14 shows the three strain field distributions at the same loading step of a load path that involves tension, out-of-plane bending and torsion about the longitudinal axis.

Figure 4.15 shows the three strain field distributions at the same loading step of a load path that involves tension, in-plane rotation and torsion about the longitudinal axis.

All predicted strain field distributions for both of these cases show that the predicted values are within 4% error of the experimental ones. This is well within the error of the RemDiS-3D experimental method.

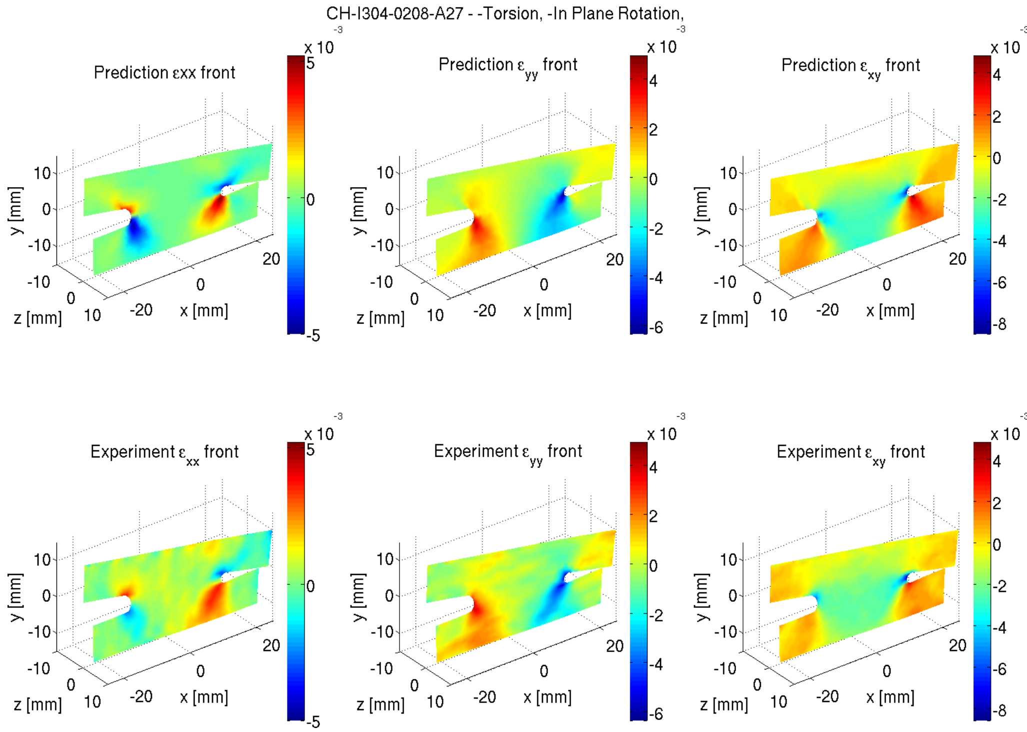

Figure 4.15: Predicted (top row) vs. experimental (bottom row) strain component fields distributions for a characterization coupon under in-plane rotation and torsion loading

---

4.6 Conclusions

We have demonstrated the application of design optimization methodologies for the determination of the constitutive response of composite materials with or without damage. Strain energy density and full field strain-based approaches have been utilized to incorporate massive full field strain measurement data from specimens loaded by a multi-axial custom-made loading machine. We have formulated objective functions expressing the difference between the experimentally observed behavior of composite materials under various loading conditions, and the simulated behavior via FEA. These formulations are expressed in terms of strain energy density functions.

In particular, two formalisms involving small strains and finite strains have been utilized in a manner that involves an additive decomposition of recoverable and irrecoverable strain energy density. This decomposition was selected in order to address both the elastic and inelastic response of composite materials due to damage. The finite strain formulation further involves an additional volumetric and distortional energy density decomposition.

Demonstrations have been given in terms of numerical examples utilizing experimental data in determining both the elastic and inelastic material parameters.

We are currently working on extending these energy formulations to approaches that achieve two main goals. First, that those approaches do not require FEA in the loop and second, that they incorporate the stochastic nature of the material response and the acquired data in a manner that quantifies uncertainty. This quantification should utilize prior knowledge via Bayesian-based stochastic formalisms, which enable incremental and recursive algorithms based on Kalman filtering and, in general, information theory.

Acknowledgments

Funding for this project was provided by the Office of Naval Research (ONR) through contracts N0001410WX20677, N0001411WX20668, N0001412WX21199 and through the Naval Research Laboratory's Basic Research Program. The authors would like to express their appreciation to Dr. I. Perez of ONR for his encouragement and support.

References

[1] J. Michopoulos, J. Hermanson, A. Iliopoulos, S. Lambrakos, and T. Furukawa, "Data-driven design optimization for composite material characterization," *Journal of Computing and Information Science in Engineering*, vol. 11, no. 2, 2011.

[2] J. Michopoulos, J. C. Hermanson, A. Iliopoulos, S. Lambrakos, and T. Furukawa, "Overview of constitutive response characterization for composite materials via data-driven design optimization," in *Proceedings of the ASME 2011 International Design Engineering Technical Conferences & Computers and Information in Engineering Conference IDETC/CIE, August 29-31, 2011, Washington, DC, USA*, 2011.

[3] I. M. Daniel and O. Ishai, *Engineering Mechanics of Composite Materials*. Oxford University Press, USA, 2nd ed., July 2005.

[4] L. Carlsson, D. F. Adams, and R. B. Pipes, *Experimental Characterization of Advanced Composite Materials, Third Edition*. CRC Press, 3 ed., Dec. 1986.

[5] P. Mast, L. Beaubien, M. Clifford, D. Mulville, S. Sutton, R. Thomas, J. Tirosh, and I. Wolock, "A semi-automated in-plane loader for materials testing," *Experimental Mechanics*, vol. 23, pp. 236–241, 1983. 10.1007/BF02320415.

[6] P. W. Mast, G. E. Nash, J. G. Michopoulos, R. W. Thomas, R. Badaliance, and I. Wolock, "Experimental determination of dissipated energy density as a measure of strain-induced damage in composites," Tech. Rep. Tec. Rpt. NRL/FR/6383–92-9369, Naval Research Laboratory, Washington, DC, USA, 1992.

[7] P. Mast, G. Nash, J. Michopoulos, R. Thomas, I. Wolock, and R. Badaliance, "Characterization of strain-induced damage in composites based on the dissipated energy density Part I. Basic scheme and formulation," *Theoretical and Applied Fracture Mechanics*, vol. 22, no. 2, pp. 71–96, 1995.

[8] J. Michopoulos, *Recent advances in Composite Materials: In Honor Of S.A. Paipetis*, ch. Computational and Mechatronic Automation of Multiphysics Research for Structural and Material Systems, pp. 9–21. Kluwer Academic Press, 2003.

[9] J. Michopoulos, "Mechatronically automated characterization of material constitutive respone," in *Proceedings of the 6th World Congress on Computational Mechanics (WCCM-VI)*, (Beijing China), pp. 486–491, Tsinghua University Press and Springer, September 5-10 2004.

[10] J. Michopoulos, J. Hermanson, and T. Furukawa, "Towards the robotic characterization of the constitutive response of composite materials," *Composite Structures*, vol. 86, no. 1-3, pp. 154–164, 2008.

[11] F. Pierron, G. Vert, R. Burguete, S. Avril, R. Rotinat, and M. R. Wisnom, "Identification of the orthotropic elastic stiffnesses of composites with the virtual fields method: Sensitivity study and experimental validation," *Strain*, vol. 43, no. 3, pp. 250–259, 2007.

[12] S. Cooreman, D. Lecompte, H. Sol, J. Vantomme, and D. Debruyne, "Elasto-plastic material parameter identification by inverse methods: Calculation of the sensitivity matrix," *International Journal of Solids and Structures*, vol. 44, no. 13, pp. 4329 – 4341, 2007.

[13] T. Furukawa and J. Michopoulos, "Computational design of multiaxial tests for anisotropic material characterization," *International Journal for Numerical Methods in Engineering*, vol. 74, no. 12, pp. 1872–1895, 2008.

[14] J. G. Michopoulos, A. P. Iliopoulos, and T. Furukawa, "Accuracy of inverse composite laminate characterization via the mesh free random grid method," *ASME Conference Proceedings*, vol. 2009, no. 48999, pp. 367–374, 2009.

[15] L. Bruno, F. M. Furgiuele, L. Pagnotta, and A. Poggialini, "A full-field approach for the elastic characterization of anisotropic materials," *Optics and Lasers in Engineering*, vol. 37, no. 4, pp. 417 – 431, 2002.

[16] T. Schmidt, J. Tyson, and K. Galanulis, "Full–field dynamic displacement and strain measurement using advanced 3d image correlation photogrammetry: Part 1," *Experimental Techniques*, vol. 27, no. 3, pp. 47–50, 2003.

[17] J. Kajberg and G. Lindkvist, "Characterisation of materials subjected to large strains by inverse modelling based on in-plane displacement fields," *International Journal of Solids and Structures*, vol. 41, no. 13, pp. 3439 – 3459, 2004.

[18] M. H. H. Meuwissen, C. W. J. Oomens, F. P. T. Baaijens, R. Petterson, and J. D. Janssen, "Determination of the elasto-plastic properties of aluminium using a mixed numerical-experimental method," *Journal of Materials Processing Technology*, vol. 75, no. 1-3, pp. 204 – 211, 1998.

[19] J. Molimard, R. Le Riche, A. Vautrin, and J. Lee, "Identification of the four orthotropic plate stiffnesses using a single open-hole tensile test," *Experimental Mechanics*, vol. 45, pp. 404–411, 2005. 10.1007/BF02427987.

[20] J. G. Michopoulos and A. P. Iliopoulos, "A computational workbench for remote full field 2d displacement and strain measurements," *ASME Conference Proceedings*, vol. 2009, no. 48999, pp. 55–63, 2009.

[21] N. P. Andrianopoulos and A. P. Iliopoulos, "Displacements measurement in irregularly bounded plates using mesh free methods," in *Proc. 16th European Conference of Fracture, Alexandroupolis, Greece, July 3–7*, 2006.

[22] A. P. Iliopoulos, J. G. Michopoulos, and N. P. Andrianopoulos, "Performance sensitivity analysis of the Mesh-Free Random Grid method for whole field strain measurements," *ASME Conference Proceedings*, vol. 2008, no. 43277, pp. 545–555, 2008.

[23] A. P. Iliopoulos, J. G. Michopoulos, and N. P. Andrianopoulos, "Performance analysis of the Mesh-Free Random Grid Method for full-field synthetic strain measurements," *Strain*, p. In Print, 2010.

[24] A. Iliopoulos and J. Michopoulos, "Sensitivity analysis of the mesh-free random grid method for measuring deformation fields on composites," in *Proceedings of the 17th International Conference on Composite Materials, ICCM-17, Edinburgh*, The British Composites Society: Edinburgh International Convention Centre (EICC), Edinburgh, UK, 2009, 27–31 Jul 2009.

[25] A. P. Iliopoulos and J. G. Michopoulos, "Effects of anisotropy on the performance sensitivity of the Mesh-Free random grid method for whole field strain measurement," *ASME Conference Proceedings*, vol. 2009, pp. 65–74, Jan. 2009.

[26] J. G. Michopoulos, J. C. Hermanson, and A. Iliopoulos, "Towards a recursive hexapod for the multidimensional mechanical testing of composites," *ASME Conference Proceedings*, vol. 2010, no. 44113, pp. 91–99, 2010.

[27] J. Michopoulos and T. Furukawa, "Multi-level coupling of dynamic data-driven experimentation with material identification," *Lecture Notes in Computer Science (including subseries Lecture Notes in Artificial Intelligence and Lecture Notes in Bioinformatics)*, vol. 4487 LNCS, pp. 1180–1188, 2007.

[28] T. Furukawa, J. Michopoulos, and D. Kelly, "Elastic characterization of laminated composites based on multiaxial tests," *Composite Structures*, vol. 86, no. 1-3, pp. 269–278, 2008.

[29] H. Man, T. Furukawa, and D. Kellermann, "Implicit constitutive modeling based on the energy principles," in *Proceedings of XXII ICTAM, 25-59 August 2008, Adelaide 2008*, 2008.

[30] T. Furukawa and J. Michopoulos, "Online planning of multiaxial loading paths for elastic material identification," *Computer Methods in Applied Mechanics and Engineering*, vol. 197, no. 9-12, pp. 885–901, 2008.

[31] J. Michopoulos, T. Furukawa, and S. Lambrakos, "Data-driven characterization of composites based on virtual deterministic and noisy multiaxial data," in *2008 ASME International Design Engineering Technical Conferences and Computers and Information in Engineering Conference, DETC 2008*, vol. 3, (New York City, NY), pp. 1095–1106, 2009.

[32] T. Furukawa and J. W. Pan, "Stochastic identification of elastic constants for anisotropic materials," *International Journal for Numerical Methods in Engineering*, vol. 81, no. 4, pp. 429–452, 2010.

[33] A. P. Iliopoulos and J. G. Michopoulos, "Loading subspace selection for multidimensional characterization tests via computational experiments," *ASME Conference Proceedings*, vol. 2010, no. 44113, pp. 101–110, 2010.

[34] R. Haj-Ali and H.-K. Kim, "Nonlinear constitutive models for FRP composites using artificial neural networks," *Mechanics of Materials*, vol. 39, no. 12, pp. 1035 – 1042, 2007.

[35] P. Haupt, *Continuum Mechanics and Theory of Materials*. Springer, 2nd ed., Apr. 2002.

[36] F. Van Der Meer and L. Sluys, "Continuum models for the analysis of progressive failure in composite laminates," *Journal of Composite Materials*, vol. 43, no. 20, pp. 2131–2156, 2009.

[37] J. W. Ju, J. Chaboche, and G. Z. Voyiadjis, *Damage Mechanics in Engineering Materials*. Elsevier Science, 1st ed., Jan. 1998.

[38] M. Kaliske, "A formulation of elasticity and viscoelasticiy for fibre reinforced material at small and finite strains," *Comput. Meth. Appl. Mech. Eng.*, vol. 185, pp. 225—-243, 2000.

[39] J. Michopoulos and A. Iliopoulos, "A computational workbench for remote full field 3d displacement and strain measurements," in *Proceedings of the ASME 2011 International Design Engineering Technical Conferences & Computers and Information in Engineering Conference IDETC/CIE, August 29-31, 2011, Washington, DC, USA*, 2011.

[40] D. R. Jones, C. D. Perttunen, and B. E. Stuckman, "Lipschitzian optimization without the Lipschitz constant," *J. Optim. Theory Appl.*, vol. 79, no. 1, pp. 157–181, 1993.

[41] The Mathworks, "Matlab." http://www.mathworks.com.

[42] K. F. Ryan, "Dynamic response of graphite/epoxy plates subjected to impact loading." http://dspace.mit.edu/handle/1721.1/42982. Thesis (M.S.)–Massachusetts Institute of Technology, Dept. of Aeronautics and Astronautics, 1990.

[43] P. M. Wegner and D. F. Adams, “Verification of the combined load compression (CLC) test methods,” Tech. Rep. DOT/FAA/AR-00/26, DOT/FAA, 2000.

[44] R. Vaidya and C. Sun, “Fracture criterion for notched thin composite laminates,” *AIAA J.*, vol. 35, no. 2, pp. 311–316, 1997.

[45] P. J. Minguet, J. Dugundji, and P. Lagace, “Postbuckling behavior of laminated plates using a direct energy-minimization technique,” *AIAA Journal*, vol. 27, no. 12, pp. 1785–1792, 1989.

[46] L. B. Lessard, O. P. Eilers, and M. M. Shokrieh, “Testing of in-plane shear properties under fatigue loading,” *Journal of reinforced plastics and composites*, vol. 14, no. 9, pp. 965–987, 1995.

[47] B. Esp and W. Chan, “Two parameter approximation to the orthotropic stress concentration factor,” in *SAMPE 2008 - Long Beach, CA May 18 - 22*, 2008.

[48] Q. Bing and C. Sun, “Modeling and testing strain rate-dependent compressive strength of carbon/epoxy composites,” *Composites Science and Technology*, vol. 65, no. 15-16, pp. 2481 – 2491, 2005. 20th Anniversary Special Issue.

[49] J. Michopoulos, H. J. C., and A. Iliopoulos, “Robotic and multiaxial testing for the constitutive characterization of composites,” in *Materials Challenges in Alternative & Renewable Energy, February 26-March 1, 2012, Clearwater, FL, USA*, 2012.

[50] J. Michopoulos, J. C. Hermanson, and A. Iliopoulos, “First industrial strength multi-axial robotic testing campaign for composite material characterization,” in *Proceedings of the ASME 2012 International Design Engineering Technical Conferences & Computers and Information in Engineering Conference IDETC/CIE, August 12-15, 2012, Chicago, IL, USA*, 2012.

In: Book Chapter: Advances in Computers and Information in Engineering Research, Volume 1
ASME Press; DOI: 10.1115/1.860328_ch4; 2014